Acta Crystallographica Section B
**Structural Science**
ISSN 0108-7681

# Structural phases of hexamethylenetetramine–pimelic acid (1/1): a unified description based on a stacking model

**Manuel Gardon, Carlos B. Pinheiro and Gervais Chapuis**

Acta Crystallographica Section B
**Structural Science**
ISSN 0108-7681

# Structural phases of hexamethylenetetramine–pimelic acid (1/1): a unified description based on a stacking model

**Manuel Gardon,* Carlos B. Pinheiro and Gervais Chapuis**

Institut de Cristallographie, Université de Lausanne, BSP Dorigny, CH-1015 Lausanne, Switzerland

Correspondence e-mail: manuel.gardon@ic.unil.ch

Received 22 April 2003
Accepted 21 May 2003

The thermotropic phase diagram of 1:1 co-crystals of hexamethylenetetramine and pimelic acid (heptanedioic acid) is investigated. Three crystalline phases are identified at ambient pressure. Phase I is disordered, as revealed by diffuse rods in its diffraction pattern. When the temperature is lowered the diffuse streaks disappear in Phase II, but superstructure reflections emerge indicating an ordering process of the structure through a non-ferroic, or at least non-ferroelastic, phase transition. Phase II is mainly characterized by an unusual distribution of its reflection intensities. Phase III is reached through a ferroelastic phase transition that induces twinned domains. A model based on the stacking of an elementary layer is proposed with the aim of describing the structures in a unified framework. Depending on the value of the unique stacking parameter $\eta$, each of the different structures observed can be reproduced by this model. Its validity is then tested by a series of simulations reproducing the main features of the diffraction patterns such as the diffuse scattering streaks, the occurrence of superstructure peaks at lower temperature and twinning.

## 1. Introduction

Hexamethylenetetramine ($C_6H_{12}N_4$, also known as hexamine, urotropine or HMT) crystallizes with alkanedioic acids [HOOC$-$(CH$_2$)$_{n-2}-$COOH with $5 \leq n \leq 14$], symbolized by C$n$, to yield 1:1 adducts, hereafter termed HMT-C$n$. In all these co-crystals pure HMT layers alternate with pure C$n$ layers, forming a lamellar structure. The C$n$ chain axes are tilted with respect to the normal of the layer plane and display a herringbone-like motif. The internal cohesion of pure HMT layers is ensured by C$-$H$\cdots$N bonds, whereas van der Waals contacts are found between aliphatic chains in the pure C$n$ layers. The overall stability between layers is ensured by strong O$-$H$\cdots$N hydrogen bonds interconnecting the N atoms of HMT molecules and the carboxylic acid group of the C$n$ chains.

The HMT-C$n$ compounds are interesting because of their rich phase diagrams. Their main structural characteristics can be classified into two categories depending on the parity of the number of C atoms in the C$n$ chains. For $n$ even, the crystals exhibit incommensurate phases, as described in HMT-C8 and HMT-C10 by Bussein Gaillard *et al.* (1996) and Bussein Gaillard *et al.* (1998). Both structures show strong anharmonic modulation at room temperature and ambient pressure. They undergo lock-in phase transitions at 123 and 291 K, respectively. Only the lock-in phase of HMT-C10 has been reported up to now (Gardon *et al.*, 2001). For $n$ odd, two compounds have already been investigated: HMT-C9 (Bonin *et al.*, 2003;

Hostettler *et al.*, 1999) and HMT-C11 (Pinheiro *et al.*, 2003). These crystals exhibit a high-temperature disordered phase, as revealed by the well organized diffuse rods observed in their diffraction patterns. On decreasing the temperature, both systems undergo ferroelastic phase transitions leading to twinning. Nevertheless, the distinction between odd and even compounds is not sharp. Some characteristics of the even compounds can be found in the odd ones. Indeed, both HMT-C9 and HMT-C11 possess similar low-temperature structures that are very close to the lock-in phase structure of HMT-C10 (Gardon *et al.*, 2001). Another example is the high-temperature region of HMT-C9 where one observes unusual phenomena resulting from the competition of incommensurate phases (Gardon *et al.*, 2003).

In this work we aim to study the complete phase sequence of hexamethylenetetramine–pimelic acid (1/1), namely HMT-C7, a 1:1 co-crystal of HMT and pimelic acid [HOOC—$(CH_2)_5$—COOH]. Three solid phases have been identified by differential scanning calorimetry (DSC) measurements performed between liquid-nitrogen temperature and the melting point (Fig. 1). Phase I is orthorhombic and disordered. As already observed in Phase II of HMT-C9 (Bonin *et al.*, 2003) and Phase II of HMT-C11 (Pinheiro *et al.*, 2003), regular diffuse rods characterize its diffraction pattern and its average structure is described in the space group *Bmmb*. Phase II, stable between 313 and 285 K, possesses an ordered structure described in the space group *Pccn*, with a doubling of one lattice parameter with respect to Phase I. The diffuse streaks observed in Phase I disappear during the I $\rightarrow$ II phase transition, giving rise to an unusual distribution of intensities. Phase III, stable from 285 K down to liquid-nitrogen temperature, exhibits two twinned domains. This phase is similar to Phase III of HMT-C9 (Hostettler *et al.*, 1999). The symmetry of each twinned domain is described by the space group $P2_1/c$. In summary, HMT-C7 possesses a phase sequence similar to those observed for HMT-C9 and HMT-C11 (Fig. 2) , but with the following main exceptions:

(i) contrary to HMT-C9 and HMT-C11, there is no indication of a non-crystalline, high-temperature phase in HMT-C7;

(ii) Phase II of HMT-C7 has no equivalent in the other HMT-C*n* compounds investigated up to now;

(iii) HMT-C7 has no phase correlated to the incommensurate structures of even compounds.

We propose a unified description for the entire phase sequence of HMT-C7 based on a stacking model. As we will prove later, this one-parameter model reproduces the main features of the reciprocal space of HMT-C7: diffuse scattering rods in Phase I; unusual reflection intensity distribution in Phase II and structural twinning in Phase III.

## 2. Experimental

### 2.1. Crystal growth and calorimetric analysis

The synthesis of HMT-C7 crystals follows the same procedure as already used for the other compounds of the HMT-C*n* family. It consists of dissolving an equimolar ratio of pimelic acid (C7) and HMT in ethanol. After complete evaporation of the solvent, the resulting white powder is dissolved in acetonitrile. The crystals grow during the slow evaporation of the solvent at room temperature or slightly below, exhibiting tabular habits with a maximum surface area of 0.5 × 0.5 mm. DSC analysis of both the primary white powder and the finely ground crystals revealed two thermotropic phase transitions between 120 K and the melting-point temperature, at around 286 and 313 K, with a slight hysteresis of 2 K for the second transition (Fig. 1). Both transitions are thermodynamically reversible.

### 2.2. Data collection and reduction

The three HMT-C7 phases have been investigated by conventional X-ray diffraction on single crystals. A sample

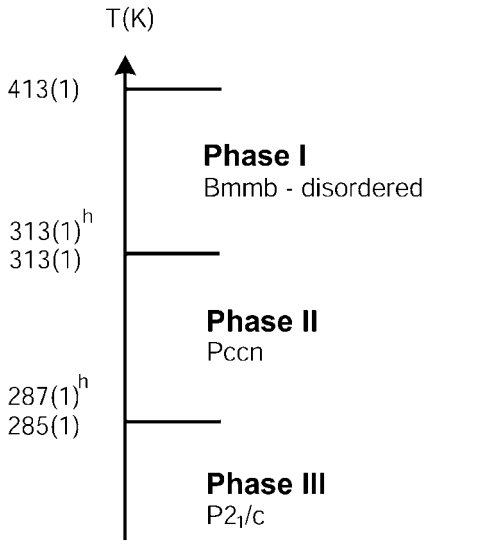


**Figure 1**
HMT-C7 phase transition sequence. Index *h* indicates temperatures determined during the heating cycle of the DSC experiment.

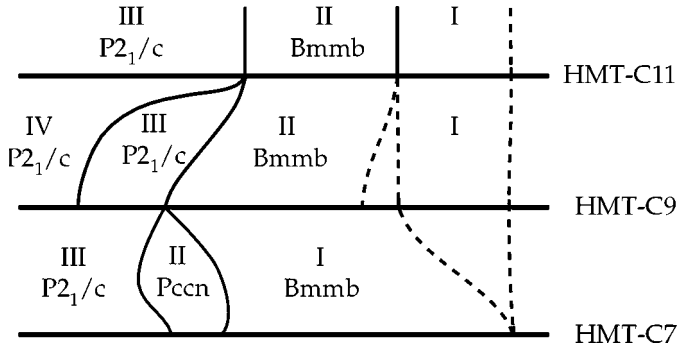


**Figure 2**
HMT-C*n* phase sequences (*n* = 7, 9, 11). The name of each phase as well as its symmetry is indicated.

**Table 1**
Experimental details.

| | Phase I | Phase II | Phase III |
|---|---|---|---|
| Crystal data | | | |
| Chemical formula | $C_7H_{12}O_4{\cdot}C_6H_{12}N_4$ | $C_7H_{12}O_4{\cdot}C_6H_{12}N_4$ | $C_7H_{12}O_4{\cdot}C_6H_{12}N_4$ |
| Chemical formula weight | 300.4 | 300.4 | 300.4 |
| Cell setting, space group | Orthorhombic, *Bmmb* | Orthorhombic, *Pccn* | Monoclinic, $P2_1/c$ |
| $a$ (Å) | 9.396 (2) | 9.5005 (4) | 5.9088 (7) |
| $b$ (Å) | 22.981 (5) | 22.660 (2) | 22.297 (2) |
| $c$ (Å) | 7.334 (2) | 14.4004 (7) | 11.856 (7) |
| $\beta$ (°) | 90 | 90 | 106.281 (7) |
| $V$ (Å$^3$) | 1583.6 (6) | 3100.1 (3) | 1499.4 (2) |
| $Z$ | 4 | 8 | 4 |
| $D_x$ (Mg m$^{-3}$) | 1.287 | 1.287 | 1.287 |
| Radiation type | Mo $K\alpha$ | Mo $K\alpha$ | Mo $K\alpha$ |
| No. of reflections for cell parameters | 3043 | 8000 | 8000 |
| $\theta$ range (°) | 3.52–25.00 | 2.32–28.02 | 2.56–27.95 |
| $\mu$ (mm$^{-1}$) | 0.096 | 0.096 | 0.099 |
| Temperature (K) | 324 (1) | 293 (1) | 120 (1) |
| Crystal form, color | Platelet, colorless | Platelet, colorless | Platelet, colorless |
| Crystal size (mm) | 0.4 × 0.4 × 0.1 | 0.2 × 0.2 × 0.1 | 0.2 × 0.2 × 0.1 |
| Data collection | | | |
| Diffractometer | Oxford-CCD; CCD | Stoe-IPDS; imaging plate | Stoe-IPDS; imaging plate |
| Data collection method | Oscillation | Oscillation | Oscillation |
| Absorption correction | None | None | None |
| No. of measured, independent and observed reflections | 3043, 749, 203 | 33 036, 3074, 1509 | 31 365, 20 129, 12 650 |
| Criterion for observed reflections | $I>2\sigma(I)$ | $I>3\sigma(I)$ | $I>3\sigma(I)$ |
| $R_{int}$ | 0.118 | 0.061 | – |
| $\theta_{max}$ (°) | 25.00 | 28.02 | 27.95 |
| Range of $h$, $k$, $l$ | $-11 \rightarrow h \rightarrow 11$<br>$-20 \rightarrow k \rightarrow 27$<br>$-8 \rightarrow l \rightarrow 7$ | $-11 \rightarrow h \rightarrow 11$<br>$-29 \rightarrow k \rightarrow 29$<br>$-18 \rightarrow l \rightarrow 18$ | $-7 \rightarrow h \rightarrow 7$<br>$-29 \rightarrow k \rightarrow 29$<br>$-15 \rightarrow l \rightarrow 15$ |
| Refinement | | | |
| Refinement on | $F^2$ | $F^2$ | $F^2$ |
| $R(F^2)$, $wR(F^2)$, $S$ | 0.1939, 0.0869, 0.707 | 0.0840, 0.1048, 1.29 | 0.0851, 0.1234, 1.53 |
| $R(F^2_{obs})$, $wR(F^2_{obs})$, $S_{obs}$ | 0.0468, 0.0647, – | 0.0387, 0.0917, 1.69 | 0.0456, 0.1070, 1.68 |
| No. of reflections and parameters used in refinements | 749, 203, 86 | 3074,1509, 260 | 20 129, 12 650, 265 |
| H-atom treatment | Riding | Mixed | Mixed |
| Weighting scheme | $w = 1/[\sigma^2(F_o^2) + (0.0192P)^2]$, $P = (F_o^2 + 2F_c^2)/3$ | $w = 1/[\sigma^2(I) + 0.0016I^2]$ | $w = 1/[\sigma^2(I) + 0.0016I^2]$ |
| $(\Delta/\sigma)_{max}$ | 0.001 | 0.0005 | 0.0014 |
| $\Delta\rho_{max}$, $\Delta\rho_{min}$ (e Å$^{-3}$) | 0.09, −0.07 | 0.26, −0.26 | 0.37, −0.37 |
| Extinction method | None | None | None |

Computer programs used: *Expose*, *Cell* (Stoe & Cie, 1997), *SHELXS* (Sheldrick & Schneider, 1997), *JANA*2000 (Petříček & Dušek, 2000).

with the dimensions 0.4 × 0.4 × 0.1 mm was selected for data collection at 324 (1) K (Phase I) on an Oxford Diffraction CCD diffractometer (Oxford Diffraction, 2000). The *Crysalis* software package (Oxford Diffraction, 2001) was used to extract the lattice parameters and the integrated intensities from the collected images. Another sample with the dimensions 0.2 × 0.2 × 0.1 mm was selected for the data collection performed at 293 (1) K (Phase II) and 120 (1) K (Phase III). These measurements were performed on a Stoe Image Plate diffractometer. The Stoe-IPDS program *Suite* (Stoe & Cie, 1997) was used to extract the lattice parameters and the integrated intensities from the collected images. The samples were cooled/heated by an external nitrogen gas stream controlled by an Oxford Cryosystem apparatus (Oxford Cryosystems, 1997). The temperature stability of the samples was better than 1 K. Mo $K\alpha$ radiation was used in all the measurements. The data-collection parameters are summarized in Table 1.[1]

**2.2.1. Phase I**. The main characteristic of the diffraction pattern is the presence of diffuse scattering rods superimposed on the Bragg reflections (Fig. 3). The diffractograms display a strong similarity with those of HMT-C9 Phase II (Bonin *et al.*, 2003) and those of HMT-C11 Phase II (Pinheiro *et al.*, 2003). The diffuse scattering and the process for modelling it will be discussed in the subsequent sections. From only the Bragg reflections, an orthorhombic *B*-centered cell with lattice parameters $a_I$ = 9.396 (2), $b_I$ = 22.981 (5) and $c_I$ = 7.334 (1) Å could be deduced from the data integration.

[1] Supplementary data for this paper are available from the IUCr electronic archives (Reference: NA5003). Services for accessing these data are described at the back of the journal.

**Table 2**
Representation of the symmetry elements which are incompatible with the three structures deduced from the stacking model.

According to the usual conventions, the planes and axis are respectively normal and parallel to the corresponding direction. The symmetry elements enclosed in parentheses ( ) are incompatible with the structural constraint 1 (the so-called 'mesh'-like pattern constraint), those in braces {} are incompatible with the constraint 2 (*i.e.* the 'herringbone'-like pattern constraint) and those in brackets [] are incompatible with the constraint 3 (*i.e.* the 'brick wall'-like pattern constraint).

| Phase I | | | Phase II | | | Phase III | | |
|---|---|---|---|---|---|---|---|---|
| **a** | **b** | **c** | **a** | **b** | **c** | **a** | **b** | **c** |
| $m$ | $m$ | $\{m\}$ | $(m)$ | $(m)$ | $\{m\}$ | | $(m)$ | |
| | $[a]$ | $\{a\}$ | | $[a]$ | $\{a\}$ | | $[a]$ | |
| $\{b\}$ | | $b$ | $\{b\}$ | | $(b)$ | | | |
| $c$ | $c$ | | $c$ | $c$ | | | $c$ | |
| $\{n\}$ | $[n]$ | $n$ | $\{n\}$ | $[n]$ | $n$ | | $[n]$ | |
| $2_1$ | $2_1$ | $2_1$ | $2_1$ | $2_1$ | $(2_1)$ | | $2_1$ | |
| 2 | $\{2\}$ | 2 | (2) | $\{2\}$ | 2 | | $\{2\}$ | |

**2.2.2. Phase II**. As illustrated in Fig. 3, the distribution of the intensities is unusual according to the extinction rules. It is nevertheless possible to simultaneously index all the reflections in a single orthorhombic cell with $a_{II}$ = 9.5005 (4), $b_{II}$ = 22.660 (2) and $c_{II}$ = 14.4004 (7) Å. It is worth noting that the diffuse scattering rods observed in Phase I have disappeared. Indeed the superstructure reflections of Phase II emerged from the diffuse scattering rods of Phase I as a result of a reordering process. Referring to the setting of Phase I, the lattice parameters of Phase II can be expressed as $\mathbf{a}_{II} \simeq \mathbf{a}_I$, $\mathbf{b}_{II} \simeq \mathbf{b}_I$ and $\mathbf{c}_{II} \simeq 2\mathbf{c}_I$ (*i.e.* inducing a doubling of the lattice parameter $\mathbf{c}_I$). The originality of Phase II is the unusual distribution of the systematic absences. Absent reflections have the Miller indices $(2n, k, 4n+2)$ and $(2n+1, k, 4n)$, with $n$ an integer. No space group can explain these unusual extinction rules. As will be shown later, a knowledge of a disorder model for Phase I will allow us to overcome this difficulty and to determine unambiguously the space group of Phase II.

**2.2.3. Phase III**. In the II → III phase transition, the symmetry decreases from orthorhombic to monoclinic and twinning induced by this change is observed. Comparison of Phase III of HMT-C7 and Phase III of HMT-C9 (Hostettler *et al.*, 1999) shows a complete similarity between their diffraction patterns. The II → III phase transition leads to twin-lattice quasi-symmetry (TLQS) twinning (Giacovazzo, 1992) with two orientational domains connected by a twofold axis or a mirror operation that is lost in the phase transition. Each superstructure reflection belongs to a single domain, while reflections corresponding to the Bragg peaks of Phase I combine reflections from both orientational domains (Fig. 3). In order to integrate simultaneously all the reflections, a monoclinic supercell with lattice parameters $a_{III}$ = 11.919 (2), $b_{III}$ = 22.607 (4), $c_{III}$ = 11.929 (2) Å and $\beta$ = 106.33 (3)° was used. The relation between the lattice parameters of Phase I and Phase III is: $\mathbf{a}_{III} \simeq \mathbf{a}_I + \mathbf{c}_I$, $\mathbf{b}_{III} \simeq \mathbf{b}_I$ and $\mathbf{c}_{III} \simeq -\mathbf{a}_I + \mathbf{c}_I$. In this monoclinic supercell the reflections can be split into three subgroups: reflections $(h\,k\,l)$ with $h = 2m$, $l = 2n+1$ ($m$, $n$ integers) belong to domain 1; reflections $(h\,k\,l)$ with $h = 2m+1$, $l = 2n$ ($m$, $n$ integers), belong to domain 2 and finally reflections $(h\,k\,l)$ with $h = 2m$ and $l = 2n$ ($m$, $n$ integers) result from the superposition of reflections belonging to both domains.

The reflection intensities of domain 1 and 2 are, respectively, given by $I_1(\mathbf{s}_1) \propto \alpha {F_1}^2$, where $\mathbf{s}_1 = (h_1\,k_1\,l_1)$ with $h_1 = 2m$ and $l_1 = 2n+1$, and $I_2(\mathbf{s}_2) \propto \beta {F_2}^2$, where $\mathbf{s}_2 = (h_2\,k_2\,l_2)$ with $h_2 = 2m+1$ and $l_2 = 2n$ ($m$, $n$ integers). The common reflection intensities are given by $I(\mathbf{s}) = I_1(\mathbf{s}_1) + I_2(\mathbf{s}_2) \propto \alpha {F_1}^2 + \beta {F_2}^2$, where $\mathbf{s} = (h\,k\,l)$ with $h = 2m$ and $l = 2n$ ($m$, $n$ integers). The $\alpha$ and $\beta$ coefficients ($\geq 0$) characterize the population factors of domains 1 and 2 (twinning ratio), and are refined with the constraint $\alpha + \beta = 1$.

The sample properties, data collection and data reduction parameters for the three phases observed so far in the HMT-C7 crystals are listed in Table 2.

## 3. Results

The diffraction patterns of Phase I show a superposition of Bragg reflections and diffuse scattering rods along the $\mathbf{a}_I^*$ direction, Fig. 3. These diffuse rods indicate a stacking disorder in the structure. Below the I → II phase transition temperature, the diffuse scattering rods condense into superstructure reflections indexed in an orthorhombic unit cell. Cooling the system below the II → III phase transition temperature, the superstructure peaks of Phase II disappear and a new set of superstructure reflections corresponding to a monoclinic lattice of Phase III emerge in between the previous ones. It is worthwhile noting that the superstructure reflections of Phases II and III emerge from the

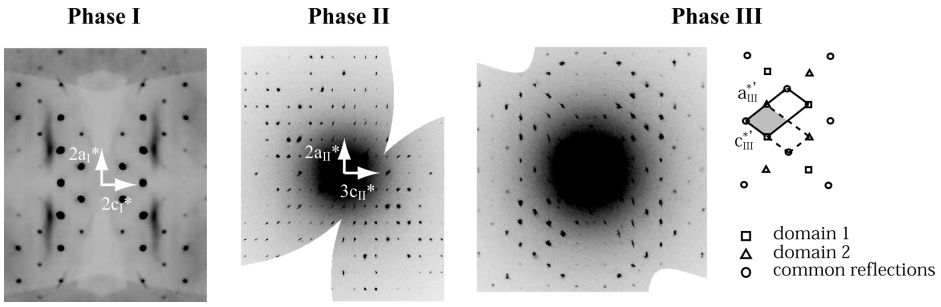


**Figure 3**
HMT-C7 reciprocal-space reconstruction of the $(h\,5\,l)$ layer for Phase I and the $(h\,4\,l)$ layer for Phases II and III. For Phase I, diffuse scattering rods along $\mathbf{a}_I^*$ are particularly visible according to $(\delta\,4\,\frac{5}{2})$, with $\delta$ continuous. Phase II is characterized by the unusual distribution of reflection intensities. Note that superstructure peaks have emerged from diffuse streaks of Phase I. Phase III together with a schematic representation of its two twinned domains is reported. The corresponding class reflections are indicated as well as the unit cell of both domains. Here again the superstructure reflections are located on the diffuse streaks of Phase I.

disappearance of diffuse scattering rods of Phase I. The superstructure reflections are certainly a consequence of the reordering of the disordered structure of Phase I. This observation suggests that the ordered structures of Phases II and III should be deduced, in a natural way, from an appropriate structural disordered model of Phase I.

### 3.1. Structure determination

**3.1.1. Stacking model**. The diffuse rods in the diffraction patterns of Phase I are observed along the $\mathbf{a}_{\rm I}^*$ direction. They exhibit the same periodicity along $\mathbf{b}_{\rm I}^*$ and $\mathbf{c}_{\rm I}^*$ as the set of Bragg reflections. They can be indexed as $(\delta, k, l+\frac{1}{2})$ with respect to the average cell $\mathbf{a}_{\rm I}, \mathbf{b}_{\rm I}, \mathbf{c}_{\rm I}$ ($\delta$ continuous, $k$ and $l$ integer indices). These diffuse-intensity rods are the expression of a stacking disorder of the structure along $\mathbf{a}_{\rm I}$ (see *e.g.* Guinier, 1967).

The ordered structures of Phases II and III of HMT-C7 can be deduced from a disordered model for Phase I which takes into account the stacking layers containing the two orientations of aliphatic C*n* chains observed in the structure refinements of the similar phases HMT-C9 and HMT-C11. This model is based on a stacking fault along $\mathbf{a}_{\rm I}$ of the elementary layer illustrated in Fig. 4. In each elementary layer two chain orientations ($A$ and $B$) alternate along the directions $\mathbf{b}_{\rm I}$ and $\mathbf{c}_{\rm I}$, forming an *ABABAB*... motif. Along $\mathbf{b}_{\rm I}$, the chains are arranged according to the herringbone pattern observed in the structures of the whole HMT-C*n* family of compounds. Referring to the setting of Phase I, the elementary layer is perpendicular to $\mathbf{a}_{\rm I}$, with thickness $\frac{1}{2}\|\mathbf{a}_{\rm I}\|$ and extends along $\mathbf{b}_{\rm I}$ and $\mathbf{c}_{\rm I}$. It possess an elementary cell with parameters $\mathbf{a}_L = \frac{1}{2}\mathbf{a}_{\rm I}$, $\mathbf{b}_L = \mathbf{b}_{\rm I}$, $\mathbf{c}_L = 2\mathbf{c}_{\rm I}$ (with $L$ referring to the layer). The elementary cell of the elementary layer is represented in Fig. 4(*a*). The two chain orientations $A$ and $B$ are arranged in such a way that their *projections* along $\mathbf{b}_L$ and $\mathbf{c}_L$ form a *mesh*-like motif, as illustrated in Figs. 4(*b*) and (*c*), respectively. Note that this assumption, far from being arbitrary, is derived from our knowledge of the structures of HMT-C9 and HMT-C11. This relevant information represents a structural constraint when determining the symmetry of the structures deduced from our stacking model. The disordered structure of Phase I is obtained by stacking the elementary layers according to the translations $\mathbf{t}_\pm = \mathbf{a}_L \pm \frac{1}{4}\mathbf{c}_L$ (*i.e.* $\mathbf{t}_\pm = \frac{1}{2}\mathbf{a}_{\rm I} \pm \frac{1}{2}\mathbf{c}_{\rm I}$), as indicated in Fig. 5(*a*). The origin of the disorder along $\mathbf{a}_{\rm I}$ in Phase I is precisely the choice, at each step of the stacking, between the two possible translational components $\pm\frac{1}{2}\mathbf{c}_{\rm I}$.

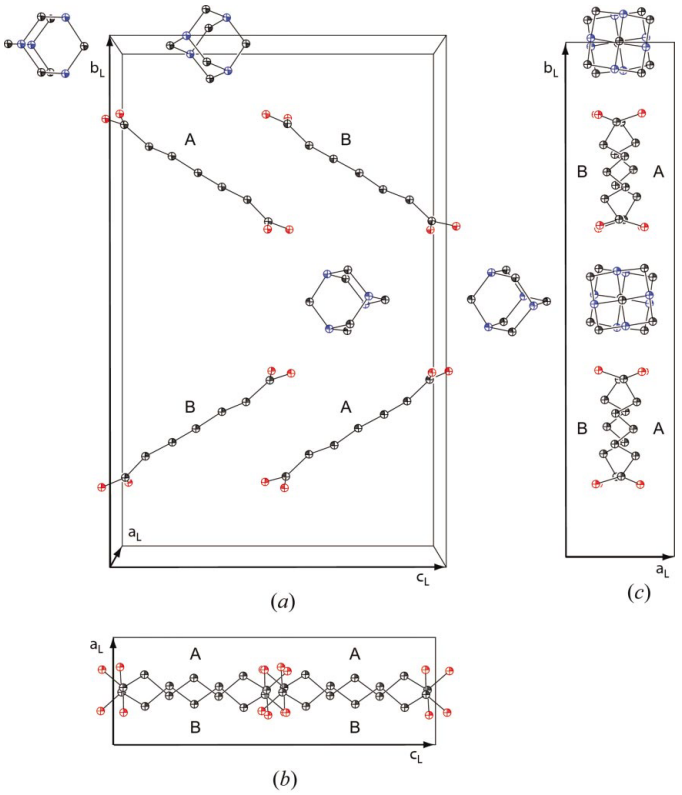


**Figure 4**
(*a*) Perspective view of the elementary layer unit cell $\mathbf{a}_L = \frac{1}{2}\mathbf{a}_{\rm I}$, $\mathbf{b}_L = \mathbf{b}_{\rm I}$, $\mathbf{c}_L = 2\mathbf{c}_{\rm I}$. The alternation of orientation chains along $\mathbf{b}_L$ and $\mathbf{c}_L$ is symbolized by $A/B$ indices. H atoms have been omitted for simplicity. (*b*) Projection of the unit cell along $\mathbf{b}_L$ showing the mesh-like pattern formed by two successive chain orientations $A$ and $B$. HMT molecules have been omitted for clarity. (*c*) Projection of the unit cell along $\mathbf{c}_L$ showing a similar mesh-like pattern.

The aim of this paper is to propose a model providing a simple and unified description of the transformations observed in the HMT-C7 structure during the heating/cooling process, rather than to develop a rigorous theory about the interactions between the C*n* molecules. With this aim, only the first and second C*n* neighbour interactions were considered. This assumption can be expressed by defining two stacking probabilities $P_1 = P(+/+) = P(-/-)$ and $P_2 = P(+/-) = P(-/+)$. $P_1$ expresses the probability of finding a translation $\mathbf{t}_+$ (or $\mathbf{t}_-$) knowing that the previous one was also $\mathbf{t}_+$ (or $\mathbf{t}_-$), *i.e.* $P_1$ is the probability of finding two layers stacked with the same translation vector $\mathbf{t}_+$ (or $\mathbf{t}_-$). $P_2$ represents the probability that the stacking sequence switches consecutively from one translation $\mathbf{t}_+$ to the other $\mathbf{t}_-$ (or $\mathbf{t}_-$ to $\mathbf{t}_+$). The probabilities are subject to the constraint $P_1 + P_2 = 1$ thus providing a stacking model with only one probability parameter $\eta = P_1$. It is worth noting that no physical behaviour of the system appears explicitly in these models. However, the definition of the probabilities and their mathematical relation are implicitly induced by the physical properties. It is known, for instance, that the temperature might influence the correlation parameters and consequently the probabilities defined in the model.

A more precise description of the structure would be achieved by taking into account the long-range interactions between the molecules. For instance, the probabilities of finding two translations $\mathbf{t}_+$ (or two $\mathbf{t}_-$) separated by $n$ layers could be introduced (see *e.g.* Wilson, 1942; Schwarzenbach, 1969). Nevertheless, such probabilistic models require some knowledge of the nature of the layer interactions and are beyond the scope of the present work.

Depending on the value of the unique parameter, $\eta \in [0,1]$, three cases are possible. For any value of $0>\eta>1$ the stacking model is able to reproduce a disordered structure with an average cell given by $\mathbf{a} = \mathbf{a}_{\rm I}$, $\mathbf{b} = \mathbf{b}_{\rm I}$ and $\mathbf{c} = \mathbf{c}_{\rm I}$. They represent the lattice parameters of the average structure of Phase I (Fig.

5*a*). For the two limiting cases $\eta = 0$ and $\eta = 1$, the stacking model reproduces two different but perfectly ordered structures. $\eta = 1$ gives rise to a monoclinic structure with lattice parameters $\mathbf{a} = \frac{1}{2}\mathbf{a}_{\rm I} + \frac{1}{2}\mathbf{c}_{\rm I} \simeq \mathbf{a}'_{\rm III}$, $\mathbf{b} = \mathbf{b}_{\rm I} \simeq \mathbf{b}_{\rm III} = \mathbf{b}'_{\rm III}$ and $\mathbf{c} = -\mathbf{a}_{\rm I} + \mathbf{c}_{\rm I} \simeq \mathbf{c}'_{\rm III}$. As can be seen from Fig. 5(*c*), this structure corresponds to one orientational domain of Phase III. In order to reproduce the coexistence of both orientational domains, it is necessary to postulate a value of $\eta$ very close to 1 but strictly different. In this case, the second domain would be given by $\mathbf{a} = \mathbf{a}_{\rm I} + \mathbf{c}_{\rm I} \approx \mathbf{a}''_{\rm III}$, $\mathbf{b} = \mathbf{b}_{\rm I} \approx \mathbf{b}''_{\rm III}$ and $\mathbf{c} = -\frac{1}{2}\mathbf{a}_{\rm I} + \frac{1}{2}\mathbf{c}_{\rm I} \approx \mathbf{c}''_{\rm III}$. Note that the domain walls, which were deduced from the model, are oriented parallel to $\mathbf{a}_{\rm III} + \mathbf{c}_{\rm III}$, *i.e.* parallel to (1 0 1), as observed by Hostettler *et al.* (1999). The second case, $\eta = 0$, describes the orthorhombic structure shown in Fig. 5(*b*), with lattice parameters $\mathbf{a} = \mathbf{a}_{\rm I} \simeq \mathbf{a}_{\rm II}$, $\mathbf{b} = \mathbf{b}_{\rm I} \simeq \mathbf{b}_{\rm II}$ and $\mathbf{c} = 2\mathbf{c}_{\rm I} \simeq \mathbf{c}_{\rm II}$. We *assume* here that the structure of HMT-C7 Phase II is the simple orthorhombic structure deduced from the stacking model with $\eta = 0$.

### 3.2. Space-group assignments

In the previous section, it was shown that the stacking model discussed above successfully predicted the crystal system and the lattice parameters of the three phases observed in HMT-C7 upon cooling/heating. The space groups for Phases I and III (*Bmmb* and $P2_1/c$, respectively) can be directly derived from the analysis of the extinction rules. Nevertheless, no conventional method was able to predict the orthorhombic space group describing the symmetry of Phase II.

In order to validate the stacking model, we shall show that there is an agreement between the symmetry of the structures generated by the model and those deduced from the experimental data. In other words, we shall show that the space groups obtained from the stacking model (in direct space) and from the experiments (in reciprocal space) indeed coincide. The assignment of the space groups was carried out using a deductive procedure which consists of eliminating step-by-step all the symmetry elements incompatible with the structural constraints imposed by the stacking model. The starting point is thus to provide such constraints that the crystal systems of Phases I and II are orthorhombic and the crystal system of Phase III is monoclinic. There are essentially three major constraints:

(i) There is an alternation of two chain orientations *A* and *B* along both **b** and **c**, such that their projections form a *mesh*-like pattern (Figs. 4*b* and *c*). This constraint is imposed by how easily the two chain orientations can be distinguished and is already found in an elementary layer.

(ii) The chain axes of the C7 molecules are parallel within a C7 layer and are tilted with respect to **b**, displaying a *herringbone*-like pattern in the **a** projection (Fig. 4*a*). This constraint is independent of the *A*/*B* chain orientations and is already found in a elementary layer.

(iii) The stacking sequence of the elementary layers is accomplished by the translations $\mathbf{t}_{\pm} = \mathbf{a}_L \pm \frac{1}{4}\mathbf{c}_L$, forming a *brick wall*-like pattern in the **b** projection (Fig. 5). This constraint is independent of the *A*/*B* chain orientations. It is not observed in an elementary layer but is related to the stacking.

The symmetry elements incompatible with the above mentioned constraints are indicated in Table 2 for each phase. The symmetry elements enclosed in parentheses ( ) are incompatible with constraint (i), those in braces { } are incompatible with constraint (ii), and those in brackets [ ] are

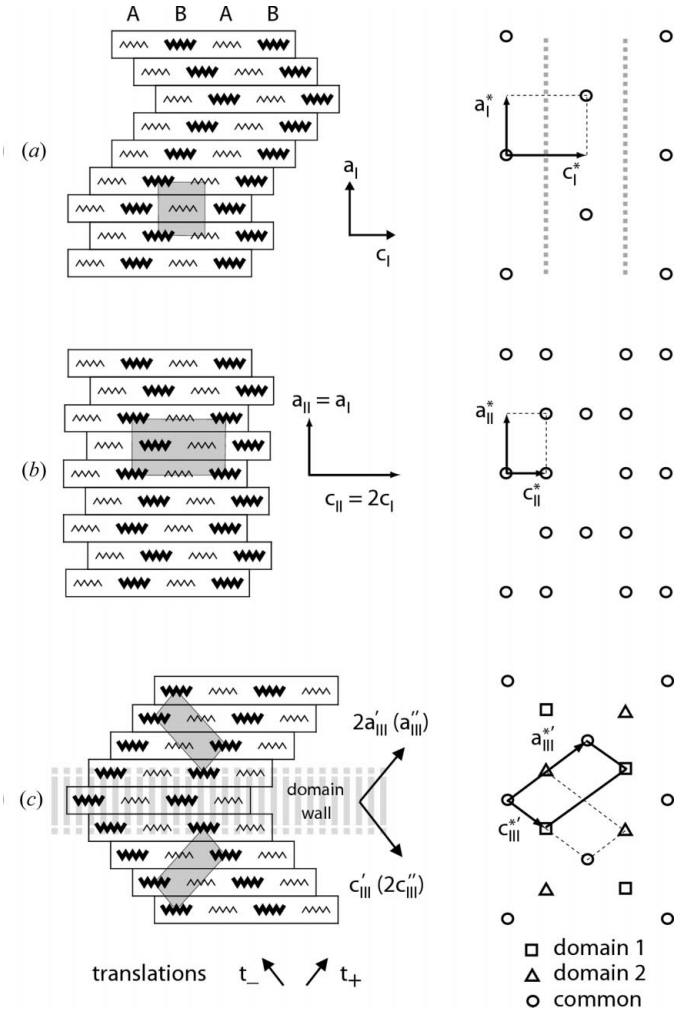


**Figure 5**
Representation of the three different stacking sequences deduced from the model. The left-hand schemes represent the cross sections perpendicular to $\mathbf{c}_L$ of the corresponding stacking sequence along $\mathbf{a}_L$. Each rectangle (each containing an *ABAB* sequence) symbolizes the cross section of two unit cells. The right-hand schemes represent the corresponding reciprocal lattice. The stacking translations $\mathbf{t}_{\pm} = \mathbf{a}_L \pm \frac{1}{4}\mathbf{c}_L$ are also indicated by arrows. (*a*) The structure of Phase I resulting from a sequence of translations constrained by a given probabilistic parameter $\eta$. The diffuse scattering streaks are schematized by dashed lines in the reciprocal-lattice representation. (*b*) The structure of Phase II resulting from a perfect alternating sequence of translations $\mathbf{t}_+$ and $\mathbf{t}_-$. The unusual absence distribution is well emphasized on the reciprocal-lattice representation. (*c*) The structure of Phase III where ordered domains appear owing to the large probability of having a sequence of the same translation $\mathbf{t}_+$ or $\mathbf{t}_-$. The domain walls corresponding to the interface between orientational domains can also be reproduced. The cells of both orientational domains are indicated. The corresponding reciprocal unit cells are reported together with the different class of reflections.

incompatible with constraint (iii). It is important to note that constraint (i) is not applicable to Phase I. Indeed, because of the average character of its structure the mesh-like pattern is already satisfied. There is no alternation of the two-chain orientations along $\mathbf{b}_L$ and $\mathbf{c}_L$, but a simple succession of the superposition of both orientations *A* and *B* (each orientation having an occupational parameter value of $\frac{1}{2}$). As a consequence, there are no symmetry elements enclosed in parentheses for Phase I. As Phase III is monoclinic with the unique $\mathbf{b}_{III}$ axis, there are no symmetry elements associated with both the $\mathbf{a}_{III}$ and $\mathbf{c}_{III}$ axes. Finally, the highest-symmetry space groups deduced from the stacking model are *Bmmb*, *Pccn* and $P2_1/c$ for Phases I, II and III, respectively. The space groups of Phases I and III are those found during the data-reduction procedure, however, the space group *Pccn* can only be definitely accepted, or rejected, after the refinements. In any case, the space group of Phase II will be one of the maximal subgroups of *Pccn*: *Pccn*, *Pcc*2, $Pc2_1n$ or $P2_12_12$. The eventuality of a monoclinic or triclinic symmetry is not mentioned because of the non-ferroelastic character of the I $\rightarrow$ II phase transition.

### 3.3. Structure refinement

In the structure solution and refinements, the H atoms belonging to the C7 acid chain have been refined according to a riding model (Johnson, 1970) for the methylene groups, with the displacement parameter fixed at 1.5 times the value of the isotropic displacement parameter of its parent C atom. In Phase I, only the intensities of the Bragg reflections were taken into account. The diffuse scattering was only used as a guideline for the simulations of the reciprocal space calculated by considering the stacking model presented above. In Phase I the Fourier difference maps did not indicate the positions of the H atoms linking the C7 acid chain and the HMT entities. These H atoms have then been added in the refinements according to the riding model. The initial attempts to refine Phase II and Phase III structures using the program *SHELXL* (Sheldrick & Schneider, 1997) indicated unacceptably large ADP's for the O atoms of the carboxyl groups. Following the results obtained for HMT-C11 (Pinheiro *et al.*, 2003), we proceeded with the structural refinement considering the anharmonicity in the displacement parameters of the O atoms. In these two phases we also considered the HMT molecule as a rigid unit (Terpstra *et al.*, 1993; Kampermann *et al.*, 1995; Bürgi *et al.*, 2000). This change in the refinement strategy reduced the number of refined parameters and allowed us to describe correctly the libration movement of the HMT molecules. In Phases II and III the distances between the O atoms and the other atoms are not referred to as oxygen mean positions but rather as the maximum of their probability density function, hereinafter termed O*Xm* (*X* = 1, 2, 3, 4). This is a necessary correction since in the higher-order refinements the mean and the standard deviation of the harmonic part include the anharmonic shifts (Kuhs, 1992).

**3.3.1. Phase I**. The structural model in the space group *Bmmb* was obtained by direct methods, using the *SHELXS* program (Sheldrick & Schneider, 1997). The choice of a non-standard space group simplifies the analysis of the structure once we describe all the phases with a unified set of lattice parameters. The structural model of Phase I is similar to that proposed for Phase II of HMT-C9 and Phase II of HMT-C11. It consists of an HMT molecule connected to a chain possessing two possible orientations, as illustrated in Fig. 6(*a*). The two chains are related by a mirror plane and have occupation parameters equal to 0.5 for each chain. Strong O—H···N bonds connect each chain to the HMT molecule. In the refinements, the oxygen of the carboxylic group which shares a double bond with C1, namely O2, was further split (O2*a*, O2*b*) in order to take into account its exceedingly large ADP's. All attempts to constrain the C1—O2*a* distance to a chemically acceptable value failed, resulting in non-positive definite ADP values for O2*a*. Indeed, the differences in the three components of the diagonal ADP's ($U_1 \simeq 2U_2 \simeq 5U_3$) indicate that the O2 splitting does not reproduce accurately the electron density around O2*a*. These results show that a complex disordering process takes place in the structure of Phase I. The poor quality data, the chain disorder and consequently the lack of information contained in the diffuse scattering rods limited a more detailed structural investigation of this phase.

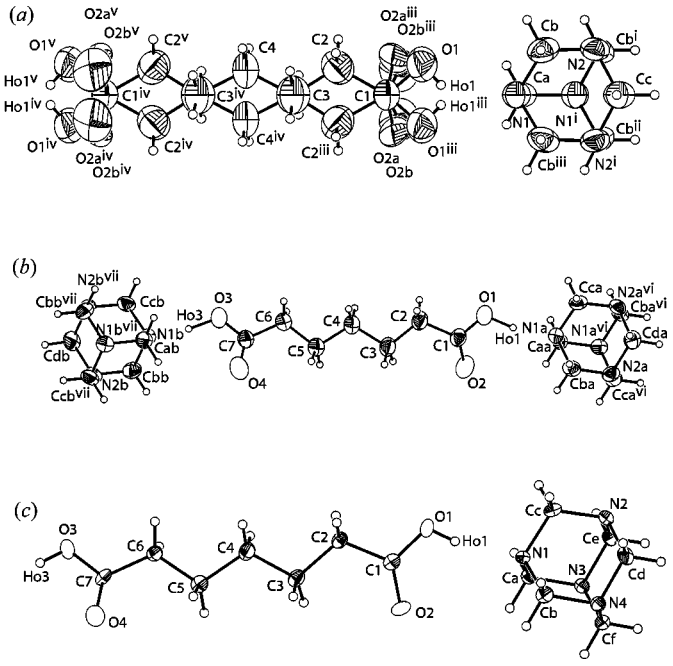


**Figure 6**
The asymmetric unit of HMT-C7 in its three distinct phases: (*a*) high-temperature disordered phase decribed in space group *Bmmb*; (*b*) ordered phase described in space group *Pccn*; (*c*) twinned phase described in space group $P2_1/c$. The atoms with superscripts are generated by applying the following symmetry operations: (i) $x, \frac{1}{2}-y, z$; (ii) $1-x, \frac{1}{2}-y, z$; (iii) $1-x, y, z$; (iv) $1-x, 1-y, 3-z$; (v) $x, 1-y, 3-z$; (vi) $\frac{1}{2}-x, \frac{1}{2}-y, z$; (vii) $\frac{1}{2}-x, \frac{3}{2}-y, z$. The symmetry operations (i), (ii), (iii), (iv), (v) refer to the space group *Bmmb* and (vi), (vii) in (*b*) refer to *Pccn*. In (*b*) and (*c*), the O atoms are represented by their approximate limiting ellipsoids.

The position and ADP's of all the atoms, except H atoms, have been refined on $wR(F^2)$ by conventional least-squares methods using the *SHELXL* program. No geometrical constraints were applied and the refined structure gave satisfactory results, despite the disordering (Table 1). The final difference-Fourier maps are flat and do not show peaks higher than $\pm$ 0.09 e Å$^{-3}$.

**3.3.2. Phase II**. The structural model in the space group *Pccn* was obtained by direct methods from the *SHELXS* program. The asymmetric unit is composed of one dicarboxylic chain connected to two half HMT molecules *via* strong O—H···N bonds (Fig. 6*b*). The structure was initially refined in the *SHELXL* program. All the atoms, except the H atoms, were refined anisotropically. The terminal O atoms of the acid groups exhibited some disorder, as evidenced by their large ADP's and the peaks found close to all the O atoms in difference-Fourier maps. As in Phase I we interpret these results as an indication of disorder. The structural refinement was further improved by considering the anharmonicity in the O atoms. In this approach the *SHELXL* model was imported into *JANA*2000 (Petříček & Dušek, 2000). The two independent half HMT molecules in the asymmetric unit have not been refined individually. Instead, a rigid half HMT model molecule has been refined in each position. The atomic coordinates of the half HMT model molecule as well as its translation and rotation parameters were adjusted during the least-squares refinement. The individual ADP's of the half HMT model molecule were replaced by the TLS tensor. Finally, the coordinates as well as the isotropic displacement parameters of the H atoms linking the HMT entities and the C7 acid chain (termed Ho1 and Ho3) were freely refined. The anharmonic model has been refined by minimizing $wR(F^2)$ using a full-matrix least-squares procedure. The final difference-Fourier maps are flat and do not show peaks higher than $\pm$ 0.26 e Å$^{-3}$. Table 1 summarizes the final statistical parameters. Selected atom distances are listed in Table 3.

Considering the key structural role played by the H atoms linking the HMT entities and the C7 acid chain, a final cycle was used to check their numerical importance to the refinements. Excluding the Ho1 and the Ho3 atoms from the final model of Phase II, the difference-Fourier map showed two peaks of 0.42 (*Mx*1) and 0.36 (*Mx*2) e Å$^{-3}$ close to O1 and O3, respectively. The third peak in the difference-Fourier map (0.26 e Å$^{-3}$) is not higher than the noise level. The *Mx*1—O1*m* distance is equal to 1.00 Å and *Mx*2—O3*m* is 1.06 Å. Furthermore, the final reliability parameters increase to $R1$ = 0.0436/0.0887 (obs/all) and to $wR$ = 0.1010/0.1168 (obs/all) in comparison to those reported in Table 1. These results clearly indicate that *Mx*1 corresponds to Ho1 and *Mx*2 corresponds to Ho3 atoms, *i.e.* at 293 K the Ho1 and Ho3 atoms were already observable in our structure refinements.

**3.3.3. Phase III**. In order to minimize the disorder in the O atoms, data collection at 120 K was performed for this refinement. The structural model in the space group $P2_1/c$ was obtained by direct methods with the help of the *SHELXS* program, using only the superstructure reflections of one domain. The solution gave the positions of all but the H atoms.

**Table 3**
Selected distances (Å) between atoms in the HMT-C7 asymmetric unit.

O*Xm* (*X* = 1, 2, 3, 4) represent the positions of the maxima of the anharmonic PDF's for the O atoms.

| Phase I | | Phase II | | Phase III | |
|---|---|---|---|---|---|
| | | O1*m*—N1*a* | 2.700 (1) | O1*m*—N1 | 2.7119 (7) |
| | | Ho1—N1*a* | 1.59 (3) | Ho1—N1 | 1.74 (1) |
| C1—O1 | 1.351 (8) | Ho1—O1*m* | 1.13 (3) | Ho1—O1*m* | 0.99 (1) |
| C1—O2*a* | 1.01 (3) | C1—O1*m* | 1.337 (2) | C1—O1*m* | 1.337 (1) |
| C1—O2*b* | 1.19 (2) | C1—O2*m* | 1.196 (2) | C1—O2*m* | 1.201 (1) |
| O2*a*—O2*b* | 0.94 (6) | C1—C2 | 1.503 (3) | C1—C2 | 1.503 (1) |
| C1—C2 | 1.499 (9) | C2—C3 | 1.516 (3) | C2—C3 | 1.534 (1) |
| C2—C3 | 1.407 (8) | C3—C4 | 1.520 (3) | C3—C4 | 1.523 (2) |
| C3—C4 | 1.432 (6) | C4—C5 | 1.518 (3) | C4—C5 | 1.530 (2) |
| N2—C*b* | 1.420 (4) | C5—C6 | 1.513 (3) | C5—C6 | 1.521 (1) |
| N2—C*c* | 1.480 (5) | C6—C7 | 1.493 (3) | C6—C7 | 1.508 (1) |
| N1—C*a* | 1.442 (4) | C7—O3*m* | 1.332 (2) | C7—O3*m* | 1.329 (1) |
| N1—C*b* | 1.489 (3) | C7—O4*m* | 1.206 (2) | C7—O4*m* | 1.197 (1) |
| O1—N1 | 2.720 (10) | Ho3—O3*m* | 1.18 (2) | Ho3—O3*m* | 1.18 (2) |
| | | Ho3—N1*b* | 1.53 (4) | Ho3—N3$^{i}$ | 1.54 (2) |
| | | O3*m*—N1*b* | 2.726 (1) | O3*m*—N3$^{i}$ | 2.696 (1) |

Symmetry code: (i) $-1-x, \frac{1}{2}+y, -\frac{1}{2}-z$.

The asymmetric unit contains one HMT-C7 entity (Fig. 6*c*). No atoms occupy special positions. The structure was further refined using the common and superstructure reflections of domains 1 and 2 simultaneously in the *SHELXL* program. The coordinates of all the heavy atoms, their harmonic ADP's and the twin volume ratio were refined by the least-squares procedure. At this point only the O2 atom presented pronounced ADP's. No indication of disorder was found around the three other independent O atoms. As in Phase II, we used the *SHELXL* model as the starting model for the anharmonic refinement. The supercell reflections and the starting model were then imported into *JANA*2000. The same refinement strategy used in Phase II was adopted in this phase. For the sake of consistency, all the O atoms were refined with anharmonic displacements. The coordinates as well as the isotropic displacement parameters of the H atoms linking the HMT cages and the C7 acid chain (Ho1 and Ho3) were freely refined. The *JANA* model refinement was carried out by minimizing $wR(F^2)$ using a full-matrix least-squares procedure. Table 1 summarizes the final refinement results. Selected distances between atoms are listed in Table 3.

**3.3.4. O—H···N bonds**. In both Phases II and III the H atoms in the O—H···N bridges were freely refined and this allowed us to determine the acid character of each end of the C7 chains. Fig. 7 summarizes the bond distances found in the carboxylic group. Note that even considering the anharmonic effects the distances between C1—O1*m* and C7—O3*m* are slightly ($\approx$ 0.03 Å) longer than the average value (C=O $\simeq$ 1.308 Å) and that the distances between C1—O2*m* and C7—O4*m* are slightly ($\simeq$ 0.02 Å) shorter than the average value (C=O $\simeq$ 1.214 Å). It seems that in addition to the anharmonicity, the COOH group might also experience a libration movement which was not taken into account during the refinements. In the refinement of HMT-C7 we confirmed a characteristic which is present in all the components of the HMT-C*n* family studied to date. Remarkably, the hydrogen

bonds linking the C7 carboxylic acid and HMT molecules of each end of the chain have different lengths: O1*m*—Ho1 = 0.99 (1) Å and O3*m*—Ho3 = 1.18 (2) Å at 120 K. This suggests a higher acid character at one end. In other words, the chain can somehow be considered as directional. There is no ambiguity in the distinction between the single C—O and double C═O bonds in the COOH molecule, as observed for the pure C7 acid crystals (Housty, 1968). From 293 K down to 120 K all except the O—H bonds change only $\sim \pm 0.02$ Å. The O—H bonds in the same temperature range decrease $\sim -0.2$ Å, *i.e.* ten times the change in the other distances. As already observed in the HMT-C11 compound, the acidity of HMT-C7 seems to be temperature dependent and no delocalization of the H atoms was observed (no peaks were found close to the N atoms).

### 3.4. Simulations

Simulations of the proposed model with different stacking sequences were performed with the program *DISCUS* (Proffen & Neder, 1997). An elementary layer consisting of 25 unit cells (or 50 alternating *A*/*B* chains) along both $\mathbf{b}_L$ and $\mathbf{c}_L$ was built. The positions of all the C, N and O atoms for both orientations were taken from the refinement of HMT-C7 Phase II. The H atoms were not included in the simulations since their contribution to the diffraction is negligible. Besides, the disordered O atoms were averaged in order to obtain only one orientation for each carboxylic group. A total of 52 500 atoms per layer were considered in the simulation. In addition, 50 elementary layers were stacked in $\mathbf{a}_L$ using values of the probabilistic $\eta$ parameter in the range $0.1 \geq \eta \geq 0.9$.

The resulting diffraction pictures were compared with the experimental observations. All values of $\eta$ in the range $0.1 \geq \eta \geq 0.9$ preserve the actual location of the diffuse scattering rods but lead to a different distribution of intensities. It was found that values of the parameter $\eta$ in the interval [0.35, 0.40] gave the best agreement for the observed diffuse scattering. These values tend to favour rather an alternation between both translations $\mathbf{t}_+$ and $\mathbf{t}_-$. Fig. 8(*a*) shows the diffractogram of the ($h$ 5 $l$) layer calculated according to this interval of probabilities and the observed pattern. Both the main peaks as well as the strongest diffuse rod along the ($\delta$ 5 $\frac{5}{2}$) direction are reproduced. The simulations did not take into account the thermal displacements of the atoms. This is the reason why the intensity fall-off with $\sin\theta/\lambda$ was not reproduced.

A model with the same dimensions (25 × 25 × 50 units) used for Phase I was adopted for the simulations of Phases II and III. The value of probabilities were $\eta = 0.01$ and $\eta = 0.99$ for Phases II and III, respectively. The choice of parameter similar to but strictly different from 1 (*i.e.* $\eta = 0.99$) allows the creation of the two domains in the calculated structure of Phase III. This model is schematized in Fig. 5(*c*), showing the domain wall at the interface between two orientational domains.

The calculated diffraction patterns of the ($h$ 4 $l$) layer of Phase II (Fig. 8*b*) and Phase III (Fig. 8*c*) reproduce the

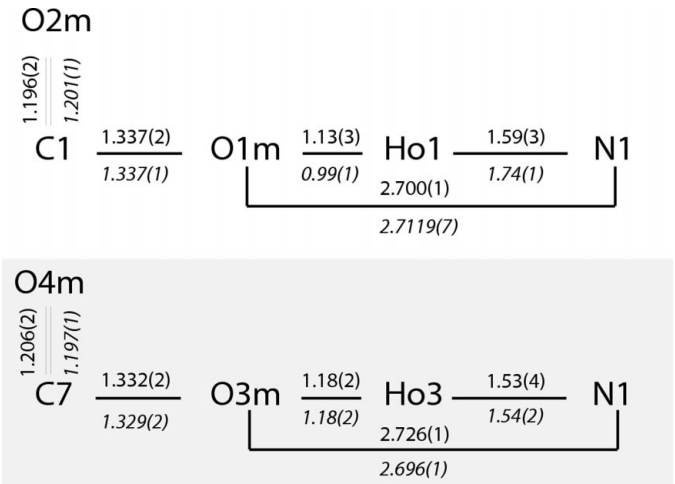


**Figure 7**
Refined O═C—O—H···N bond distances (Å) of the acid group at 293 and 120 K. Distances refined at 120 K are represented by italic numbers. O*Xm* (*X* = 1, 2, 3, 4) indicate the positions of the maxima of the oxygen PDF's.

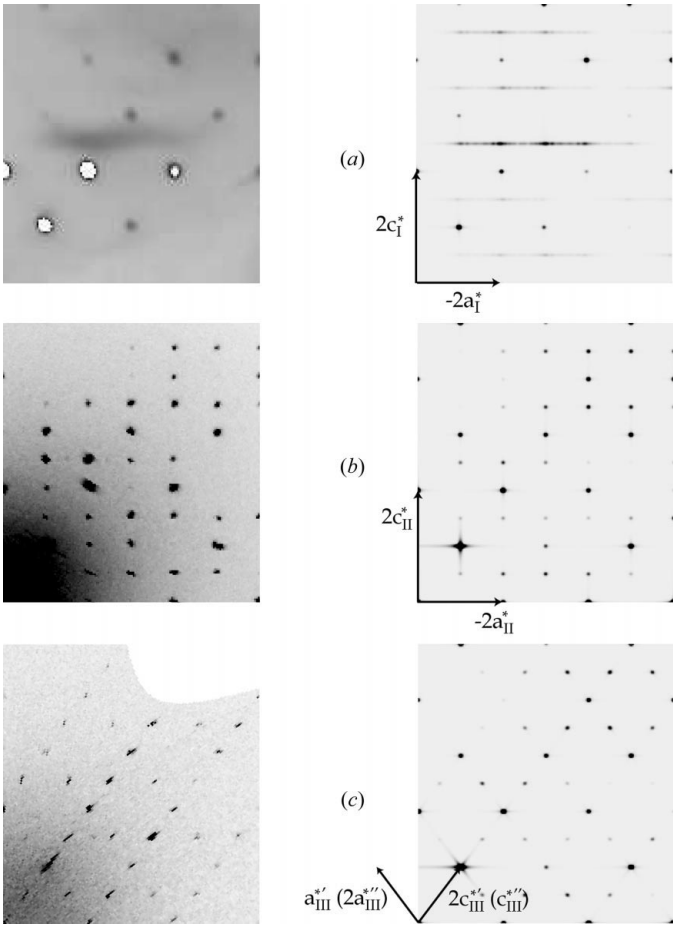


**Figure 8**
Comparison of (*a*) the ($h$ 5 $l$) layers of Phase I, (*b*) the ($h$ 4 $l$) layers of Phase II and (*c*) the ($h$ 4 $l$) layers of Phase III between the observed diffraction patterns and the result of the corresponding simulations.

maximum intensities at the positions of the Bragg peaks and the superstructure reflections. The particular intensity distribution of Phase II is well reproduced as well as the three reflection classes of Phase III (common plus domains 1 and 2). Owing to the symmetric probabilities, *i.e.* $P(+/+) = P(-/-)$, the volume ratio between the two orientational domains is $\simeq 0.5$. We believe that the difference in volume ratio observed in real crystals is a consequence of the kinetic factors in the transition or because of the frustration induced by the gluing of the sample to the needle.

## 4. Conclusion

The stacking model proposed for the different HMT-C7 phases reproduces qualitatively the observed diffraction patterns. Both the main reflections as well as the diffuse rods could be simulated. The symmetry *Bmmb* of Phase I and the symmetry $P2_1/c$ of Phase III predicted by the analysis of the extinction rules were successively reproduced by the stacking model. In addition, the space group *Pccn* of Phase II has been obtained from the model alone. In view of the similarities already evoked between HMT-C7, HMT-C9 and HMT-C11, it is also possible to describe the structures of Phase II and III of HMT-C9 and that of Phase II of HMT-C11 by the stacking model. Indeed the thermotropic phase sequences of both HMT-C9 and HMT-C11 do not fit completely in the descriptive scheme proposed for HMT-C7; they both possess a low-temperature phase (Birkedal *et al.*, 2003; Pinheiro *et al.*, 2003) which cannot be deduced by a stacking of the elementary layers defined in our model. The basic entity of the model is the elementary layer which possesses some symmetry constraints, like the alternation of the two chain orientations *A*/*B* along both $\mathbf{b}_I$ and $\mathbf{c}_I$ directions. Such construction translates in reality to a strong correlation of the structure along $\mathbf{b}_I$ and $\mathbf{c}_I$, whereas, depending on the stacking sequence of the layers, a short- (Phase I) or long-range order (Phases II and III) can be observed along $\mathbf{a}_I$. The fact that the elementary layer is conserved during the phase transitions (despite the different stacking sequence) can be interpreted as the expression of a common transformation mechanism which maintains the internal structure of each layer. From this viewpoint, the phase transitions III $\rightarrow$ IV in HMT-C9 and II $\rightarrow$ III in HMT-C11 are driven by different mechanisms which induce new competitive interactions that destroy or rearrange the hierarchy of correlations. The origin of such differing mechanisms, depending on the increasing number *n* of C atoms in the C*n* chain, can be correlated to the chain torsion. Indeed, it has been seen in HMT-C11 (Pinheiro *et al.*, 2003) that the torsion of the chain around its internal axis changes discontinuously during the II $\rightarrow$ III transition and increases during the cooling. This process induces a different topology of the end COOH acid groups with respect to the HMT molecules. Consequently, a redistribution of the O—H$\cdots$N and C—H$\cdots$O interactions is expected, implying a modification of the overall correlations in the structure.

This work was supported by the Swiss National Science Foundation grant 20.56870.99. We thank Dr Vaclav Petříček for the help with *JANA*2000, Professor Dieter Schwarzenbach for helpful discussions and Dr Kurt Schenk for the critical reading of this manuscript. MG is grateful to the Swiss National Science Foundation for a one-year grant in Vienna.

## References

Birkedal, H., Gardon, M., Hostettler, M., Schwarzenbach, D., Chapuis, G. & Bonin, M. (2003). In preparation.
Bonin, M., Welberry, T. R., Hostettler, M., Gardon, M., Birkedal, H., Chapuis, G., Möckli, P., Ogle, C. A. & Schenk, K. J. (2003). *Acta Cryst.* B**59**, 72–86.
Bürgi, H. B., Capelli, S. C. & Birkedal, H. (2000). *Acta Cryst.* A**56**, 425–435.
Bussien Gaillard, V., Chapuis, G., Dušek, M. & Petříček, V. (1998). *Acta Cryst.* A**54**, 31–43.
Bussien Gaillard, V., Paciorek, W., Schenk, K. & Chapuis, G. (1996). *Acta Cryst.* B**52**, 1036–1047.
Gardon, M., Schenk, K. J., Bonin, M. & Tolédano, P. (2003). Submitted for publication.
Gardon, M., Schönleber, A., Chapuis, G., Hostettler, M. & Bonin, M. (2001). *Acta Cryst.* C**57**, 936–938.
Giacovazzo, C. (1992). *Fundamentals of Crystallography*, ch. 2, pp. 83–87. Oxford University Press.
Guinier, A. (1967). *X-ray Diffraction by Perfect and Disordered Crystals.* San Francisco: Freeman Publishing.
Hostettler, M., Birkedal, H., Gardon, M., Chapuis, G., Schwarzenbach, D. & Bonin, M. (1999). *Acta Cryst.* B**55**, 448–458.
Housty, J. (1968). *Acta Cryst.* B**24**, 486–494.
Johnson, C. K. (1970). *Crystallographic Computing*, edited by F. R. Ahmed, pp. 207–220. Copenhagen: Munksgaard.
Kampermann, S. P., Sabine, T. M., Cravens, B. M. & McMullan, R. K. (1995). *Acta Cryst.* A**51**, 489–497.
Kuhs, W. F. (1992). *Acta Cryst.* A**48**, 80–98.
Oxford Cryosystems (1997). *Oxford Cryostream Cooler*, 600 series. Oxford Cryosystems, Oxford, UK; http://www.oxfordcryosystems.co.uk.
Oxford Diffraction (2000). *Xcalibur Single Crystal CCD Diffractometer.* Oxford Diffraction Sp.Zo.o, Wroclaw, Poland; http://www.oxford-diffraction.com.
Oxford Diffraction (2001). *Xcalibur Single Crystal CCD Diffractometer, CrysAlis Software Package*, Version 1.167. Oxford Diffraction Sp.Zo.o, Wroclaw, Poland; http://www.oxford-diffraction.com.
Petříček, V. & Dušek, M. (2000). *The Crystallographic Computing System JANA2000.* Institute of Physics of the Academy of Science of the Czech Republic, Prague, Czech Republic.
Pinheiro, C. B., Gardon, M. & Chapuis, G. (2003). *Acta Cryst.* B**59**, 416–427.
Proffen, T. & Neder, R. B. (1997). *J. Appl. Cryst.* **30**, 171–175.
Schwarzenbach, D. (1969). *Z. Kristallogr.* **128**, 97–114.
Sheldrick, G. M. & Schneider, T. R. (1997). *Methods Enzymol.* **277**, 319–343.
Stoe & Cie (1997). *IPDS Software Manual*, Version 2.87. Stoe and Cie GmbH, Darmstadt, Germany; http://www.stoe.com.
Terpstra, M., Craven, B. M. & Stewart, R. F. (1993). *Acta Cryst.* A**49**, 685–692.
Wilson, A. J. C. (1942). *Proc. R. Soc. London Ser. A*, **180**, 277–285.